

MORPHOLOGY OF GAMMA-RAY HALOS AROUND MIDDLE-AGED PULSARS: INFLUENCE OF THE PULSAR PROPER MOTION

YI ZHANG^{1,2}, RUO-YU LIU^{1,2}, S. Z. CHEN^{3,4}, XIANG-YU WANG^{1,2}

¹School of Astronomy and Space Science, Xianlin Road 163, Nanjing University, Nanjing 210023, China; ryliu@nju.edu.cn; xywang@nju.edu.cn

²Key laboratory of Modern Astronomy and Astrophysics (Nanjing University), Ministry of Education, Nanjing 210023, People's Republic of China

³ Key Laboratory of Particle Astrophysics, Institute of High Energy Physics, Chinese Academy of Sciences, 100049 Beijing, China

⁴TIANFU Cosmic Ray Research Center, Chengdu, Sichuan, China

ABSTRACT

Recently, γ -ray halos of a few degree extension have been detected around two middle-aged pulsars, Geminga and PSR B0656+14 by the High Altitude Water Cherenkov observatory (HAWC). The measurements of surface brightness profile of the pulsar halos suggest that the transport of particles therein is dominated by diffusion, and the diffusion coefficient is significantly lower than the average value in the Galactic disk. Since pulsars typically have a proper velocity of 400 – 500 km/s, the displacement of these middle-aged pulsars due to the proper motion could be important in shaping the morphology of the pulsar halos. Motivated by this, we study the morphology of pulsar halos considering proper motion in the diffusion-dominated scenario. We find that the morphology of the pulsar halo can be basically classified into three evolutionary phases, depending on the velocity of the proper motion, cooling of the emitting electrons and the age of the pulsar. Generally, the morphology would appear highly asymmetric at $\lesssim 1$ TeV while keeps more or less spherical at $\gtrsim 10$ TeV for middle-aged pulsars. We also study the offset between the position of pulsars and the center of the intensity map of the corresponding halo. We find that proper motion can induce observable offsets seen by Fermi-LAT, HESS, HAWC and LHAASO from GeV up to a few TeV energies provided that the source is located within several kpc from Earth. It is more difficult to produce resolvable offset in the pulsar halo at higher energy due to more rapid cooling of emitting electrons. Our result can provide constraints on the origins of those extended sources at very high energies.

1. INTRODUCTION

Pulsar wind nebulae (PWNe) are bubbles of shocked relativistic particles (electrons and positrons,¹) accelerated when a pulsar's relativistic wind interacts with its environment, either the supernova remnant (SNR) or the interstellar medium (ISM) (Gaensler & Slane 2006). Since a pulsar is formed in a SN explosion, the pulsar and its PWN are initially surrounded by an expanding SNR. The SNR blast wave at first moves outward freely at a speed $> (5-10) \times 10^3$ km s⁻¹, while the asymmetry in the SN explosion would give the pulsar a natal velocity of 400 – 500 km s⁻¹ typically. At early epoch the pulsar is located near the SNR's center. Observationally, we expect to see a rapidly expanding SNR, with a reasonably symmetric PWN near its center, and a young pulsar at the center of the PWN.

The expanding supernova shell slows down as it accumulates material in the surrounding interstellar medium (ISM); as the supernova enters the Sedov-Taylor phase, the shell comprises both a forward and reverse shock that eventually returns inwards (Truelove & McKee 1999). The reverse shock formed in such a system may interact with the expanding

PWN, leading to a crushing effect in some cases (Reynolds & Chevalier 1984). The reverse shock reaches the PWN in a time (Reynolds & Chevalier 1984):

$$t_{\text{Sedov}} = 7 \text{ kyr} \left(\frac{M_{\text{ej}}}{10 M_{\odot}} \right)^{-5/6} \left(\frac{E_{\text{SN}}}{10^{51} \text{ erg}} \right)^{-1/2} \left(\frac{n}{1 \text{ cm}^{-3}} \right)^{-1/3} \quad (1)$$

If the SNR has expanded into an inhomogeneous medium, then the reverse shock moves inward faster on some sides than on others. γ -ray PWNe are often extended and offset from the associated pulsar (Gaensler & Slane 2006; de Jager & Djannati-Ataï 2009), an example of such a system is the Vela SNR. This evolutionary scenario is typically invoked to account for the wide variety of PWN morphology seen in these evolved systems (Aharonian et al. 2005; H. E. S. S. Collaboration et al. 2012b,a). Because the SNR is decelerating, the pulsar ultimately penetrates and then escapes the shell. After that, a pulsar proceeds to move through the ambient ISM. The pulsar will move supersonically and drive a bow shock through the ISM.

The High-Altitude Water Cherenkov Observatory (HAWC) recently reported discovery of spatially extended TeV sources surrounding two middle-aged ($t_{\text{age}} = 100 - 400$ kyr) pulsars, namely, Geminga and Monogem (or PSR B0656+14) (Abey-

¹ hereafter we do not distinguish positrons from electrons for simplicity

sekara et al. 2017, see also Abdo et al. 2009). The intensity profile of the TeV sources can be explained with the inverse Compton (IC) scatterings of diffusing electrons, which are injected from the pulsars, on the cosmic microwave background (CMB) and the interstellar radiation field (ISRF) (Abeysekara et al. 2017; López-Coto & Giacinti 2018; Tang & Piran 2019; Liu et al. 2019a,b; Di Mauro et al. 2019). The physical extension of the sources is at least 30 pc which is much larger than the size of the PWN of the corresponding pulsars, indicating that accelerated electrons escape the PWN and produce the halo-like emissions in the ambient ISM of the pulsars.

In addition to Geminga and Monogem, many more such pulsar halos could have been already detected by instruments such as HAWC, MILAGRO, HESS, Fermi-LAT and so on. The HAWC Collaboration has recently released the 2HWC catalog (Abeysekara et al. 2018) which contains 39 sources detected close to the Galactic plane. Some of them have an extended γ -ray morphology, and are spatially close to powerful Galactic pulsars of middle ages. More recently, in the new released 3HWC catalog (Albert et al. 2020) they highlight 12 extended TeV sources as the potential pulsar halos. In the reported PWNe and PWNe candidates by H. E. S. S. Collaboration et al. (2018b,a), the spatial extensions of some sources are significantly larger than 10 pc which are beyond the prediction of the dynamical evolution model for PWNe (Reynolds & Chevalier 1984; van der Swaluw et al. 2001; Bucciantini et al. 2003). Some of these sources could also be pulsar halos in nature, or a mixture of PWN and halo (e.g. Liu & Yan 2020). The Large High Altitude Air Shower Observatory (LHAASO) is a new generation instrument to study the TeV-PeV γ -ray sky (Bai et al. 2019). LHAASO contains two major γ -ray astronomic devices: the Water Cherenkov Detector Array (WCDA) and 1 km² Array (KM2A). With its great sensitivity and large-sky area monitoring capability, LHAASO will play a key role in the detection of pulsar halos at TeV-PeV band.

The morphology of the γ -ray halos is clearly an important property for identifying pulsar halos. A pulsar's proper motion may lead to a displacement of about $80(v_p/400 \text{ km s}^{-1})(t_{\text{age}}/200 \text{ kyr}) \text{ pc}$ from its birth place. Such a displacement could be larger than the spatial extension of the TeV halo for middle-aged pulsars, so it may largely affect the γ -ray morphology. Indeed, spatial offsets between the centroids of the pulsar halo candidates and the associated pulsars are commonly observed (Abeysekara et al. 2018; Albert et al. 2020; H. E. S. S. Collaboration et al. 2018b). Although the offset may be explained with the proper motion of the pulsar (H. E. S. S. Collaboration et al. 2018b; Di Mauro et al. 2020), it is not straightforward to connect a γ -ray sources and the associated pulsar in the case of large offset being detected, especially without a knowledge on the pulsar's proper motion velocity. On the other hand, various factors such as continuous injection of electrons, cooling of electrons, and the limit of the angular resolution of instruments (i.e., the PSF), could

smear out the offset, making the identification more complex.

Motivated by this, we study the effect of pulsar proper motion on the morphology of pulsar halo at GeV and TeV band. We focus on pulsar with ages of $t_{\text{age}} \gg t_{\text{Sedov}}$, so the γ -ray halos are produced by pulsar wind particles diffusing in the ISM. For comparison with observations, we simulate the counts map by convolving the model-predicted morphology with the PSF of some instrument, such as Fermi, HESS and LHAASO. The rest of the paper is organized as follows. In section 2, we introduce our model for the γ -ray emission of the pulsar halo. In section 3, we show and analyze the resulting γ -ray intensity map (morphology) of pulsar halo. In section 4 we look into the offset between the center of the pulsar halo and the pulsar's location caused by the proper motion. We discuss the result in section 5 and give our conclusion in section 6.

2. MODEL FOR THE γ -RAY EMISSION OF A PULSAR HALO

In the model of pulsar halo considered in this work, relativistic electrons are continuously injected into the ambient ISM of a pulsar. We assume that the evolution of the total electron injection rate follows the pulsar's spindown history with a braking index n (Gaensler & Slane 2006)

$$L_e(t) = \eta_e L_i (1 + t/\tau_0)^{-(n+1)/(n-1)}, \quad (2)$$

where t is the time after the pulsar's birth, η_e is the fraction of the spindown energy converted into relativistic electrons, L_i is the initial spindown luminosity of the pulsar, $\tau_0 = 2\tau_c/(n-1) - t_{\text{age}}$ is the initial spin-down timescale with τ_c being the "characteristic age". Given the present rotation period of the pulsar P , the first derivative of the period \dot{P} and the initial rotation period P_0 , we have $\tau_c = P/2\dot{P}$ and $\tau_{\text{age}} = [2\tau_c/(n-1)] [1 - (P_0/P)^{n-1}]$. Considering the Geminga pulsar as a benchmark example, we take $P = 237 \text{ ms}$, $\dot{P} = 1.1 \times 10^{-14} \text{ ss}^{-1}$ and the present spindown luminosity $L_s = 3.3 \times 10^{34} \text{ erg/s}$. Further assuming $P_0 = 50 \text{ ms}$ and the standard magnetic dipole braking (i.e., $n = 3$), we obtain $\tau_0 = 15 \text{ kyr}$, $t_{\text{age}} = 327 \text{ kyr}$ and $L_i = 3.2 \times 10^{37} \text{ erg/s}$.

We assume the injection electron spectrum to be a power-law function with an exponential cutoff, i.e.,

$$Q_e(E_e, t) = Q_0(t) E_e^{-\gamma_e} \exp\left(-\frac{E_e}{E_c}\right), \quad (3)$$

where $Q_0(t)$ is the normalization factor which can be determined by $\int E_e Q_e(E_e, t) dE_e = L_e(t)$. We consider $\eta_e = 1$, $\gamma_e = 2$ and $E_c = 400 \text{ TeV}$ as reference parameters. For simplicity, we neglect any possible influence of the PWN on the injected electrons here and following calculation.

The transport equation of electrons injected from a point source located at \mathbf{r}_s is

$$\frac{\partial n_e}{\partial t} = D(E_e) \nabla_{\mathbf{r}}^2 n_e + \frac{\partial [b(\mathbf{r}, E_e, t) n_e]}{\partial E_e} + Q_e(E_e, t) \delta^3(\mathbf{r} - \mathbf{r}_s), \quad (4)$$

where $n_e(\mathbf{r}, E_e, t)$ is the differential electron density at time

t and position \mathbf{r} , and $D(E_e)$ is the diffusion coefficient assuming isotropic diffusion, which is assumed to be spatially homogeneous and scales with the energy as $D(E_e) = D_0(E_e/1\text{GeV})^{1/3}$. We note that, based on HAWC's observation on the pulsar halos of Geminga and Monogem, it has been suggested that there may be a slow diffusion zone in the vicinity of the pulsar within a radius of $30 - 100$ pc from the pulsar while the diffusion coefficient beyond the radius is the standard one in the ISM measured from primary-to-secondary cosmic ray ratio (Fang et al. 2018; Profumo et al. 2018). For simplicity, we here do not consider the two-zone scenario but will discuss its influence on our result later. $b(\mathbf{r}, E_e, t)$ is the energy loss rate of electrons during the propagation due to the synchrotron and IC radiation. We here consider a homogeneous and constant magnetic field and radiation field. The energy loss rate, b , is given by

$$b(E_e) = -\frac{dE_e}{dt} \simeq -\frac{4}{3}\sigma_T c \left(\frac{E_e}{m_e c^2} \right)^2 \left[U_B + \frac{U_{ph}}{(1 + \frac{4E_e \epsilon_0}{m_e c^4})^{3/2}} \right], \quad (5)$$

where σ_T is the Thomson cross section, $U_B = B^2/8\pi$ is the magnetic field energy density and U_{ph} is the radiation field energy density. $\epsilon_0 = 2.82kT$ is the typical photon energy of blackbody/greybody target radiation field. We assume a homogeneous magnetic field of $B = 3\mu\text{G}$ and consider four blackbody/greybody components around the pulsar as: CMB ($T = 2.73\text{ K}$ and $U = 0.25\text{ eVcm}^{-3}$), far-infrared radiation (FIR) field ($T = 40\text{ K}$ and $U = 1\text{ eVcm}^{-3}$), near-infrared radiation field ($T = 500\text{ K}$ and $U = 0.4\text{ eVcm}^{-3}$) and visible light radiation field ($T = 3500\text{ K}$ and $U = 1.9\text{ eVcm}^{-3}$). The employed interstellar radiation field refers to the model by Popescu et al. (2017) at a smaller Galactocentric radius (i.e., $3 - 5\text{ kpc}$) given more TeV PWNe and PWN candidates appearing at such radius (H. E. S. S. Collaboration et al. 2018b).

The present-day ($t = t_{\text{age}}$) density of electrons with energy E_e at a radius r away from the pulsar can be calculated by

$$n_e(\mathbf{r}, E_e) = \int_0^{t_{\text{age}}} dt' Q_e(\mathcal{E}'_e(t'), t') \times \frac{\exp[-(\mathbf{r} - \mathbf{r}_s(t'))^2/4\lambda(E_e, t')]}{(4\pi\lambda(E_e, t'))^{3/2}} \frac{d\mathcal{E}'_e(t')}{dE_e}, \quad (6)$$

where $\lambda(E_e, t') = \int_{t'}^{t_{\text{age}}} D(E_e(t'')) dt''$ and \mathcal{E}'_e is the electron energy at injection. $E_e(t')$ represents the trajectory of energy evolution of an electron whose energy is E_e at present. The relation between $E_e(t')$ and \mathcal{E}'_e as well as $d\mathcal{E}'_e/dE_e$ can be found by tracing the energy evolution of the electron via Eq. 5. We take the cylindrical coordinate system and set the direction of the proper motion as the z -axis. The present pulsar position is set to $(0, 0, 0)$ and then the historical position of the pulsar can be given by $\mathbf{r}_s = (0, 0, v_p(t - t_{\text{age}}))$.

We then calculate the γ -ray emission produced by IC process of electrons and integrate them over line of sight at different viewing angle, following the method given by Liu et al. (2019b). For simplicity, we consider the proper motion di-

rection is perpendicular to our line of sight toward the pulsar (i.e., we assume the pulsar's velocity is parallel to the celestial plane). By doing so, the emission of the halo is projected onto the celestial plane and we obtain the γ -ray intensity at a polar angle θ from the pulsar and an azimuth angle ϕ ($\phi = 0$ points to the inverse direction of the proper motion) is $I'_\gamma(E_\gamma, \theta, \phi)$, which is the intrinsic morphology of the γ -ray halo.

We convolve I'_γ with the PSF of various instruments at different energies (summarized in Table. 1) to simulate the counts map of observation, which is the observed morphology. The γ -ray intensity profile after convolving the PSF is then given by

$$I_\gamma(E_\gamma, \theta, \phi) = \iint \frac{1}{2\pi\sigma^2} \exp\left(-\frac{d'^2}{2\sigma^2}\right) I'_\gamma(E_\gamma, \theta', \phi') \sin\theta' d\theta' d\phi'. \quad (7)$$

where $d' = \cos\theta \cos\theta' + \sin\theta \sin\theta' \cos(\phi - \phi')$ is the angular distance between (θ, ϕ) and (θ', ϕ') and $\sigma(E_\gamma)$ is the size of the PSF as a function of γ -ray energy.

3. MORPHOLOGY OF THE PULSAR HALO

We first calculate the morphology of the γ -ray halo in the benchmark case (i.e., halo of a Geminga-like pulsar). The intrinsic intensity maps of the pulsar halo at 10 GeV , 1 TeV , 10 TeV and 100 TeV , as well as the corresponding intensity profile along the axis of the pulsar's proper motion (defined as the negative x -axis), are shown in Fig. 1. It is obvious that the morphology is energy-dependent. The morphology of the pulsar halo at 10 GeV and 1 TeV is highly anisotropic, with extended emission towards the right half part where the pulsar has passed. At the GeV band, the pulsar halo is drop-shaped, with two separated bright regions. The strongest emission is around the initial pulsar position, where the relic electrons from early injection pulsar are still emitting γ -rays. This is because the cooling time of GeV -emitting electrons is longer than the age of the pulsar while the spindown luminosity of the pulsar at early epoch is much higher than that at present. On the other hand, electrons injected recently form a comparatively high electron density region around the pulsar, thus yielding another peak in the intensity profile. While for TeV -emitting electrons, their cooling time is shorter than, but still comparable to, the age of the pulsar. Therefore, the morphology of the pulsar halo at 1 TeV is extended towards $x > 0$ but peaks around the current position of the pulsar. At higher-energy (e.g., 10 TeV and 100 TeV), the relic electrons are significantly cooled so the intensity of the halo peaks at the current position of the pulsar without significant extension and the emission of halo is entirely dominated by newly injected electrons.

In order to compare with observations, we also give the intensity map and the profile after convolving the PSF of four γ -ray detectors in Fig. 2, i.e., the PSF of Fermi-LAT for 10 GeV emission, HESS for 1 TeV emission, LHAASO-WCDA for 10 TeV emission and LHAASO-KM2A for 100 TeV emission (see Table. 1). The PSF of HAWC is similar to LHAASO-

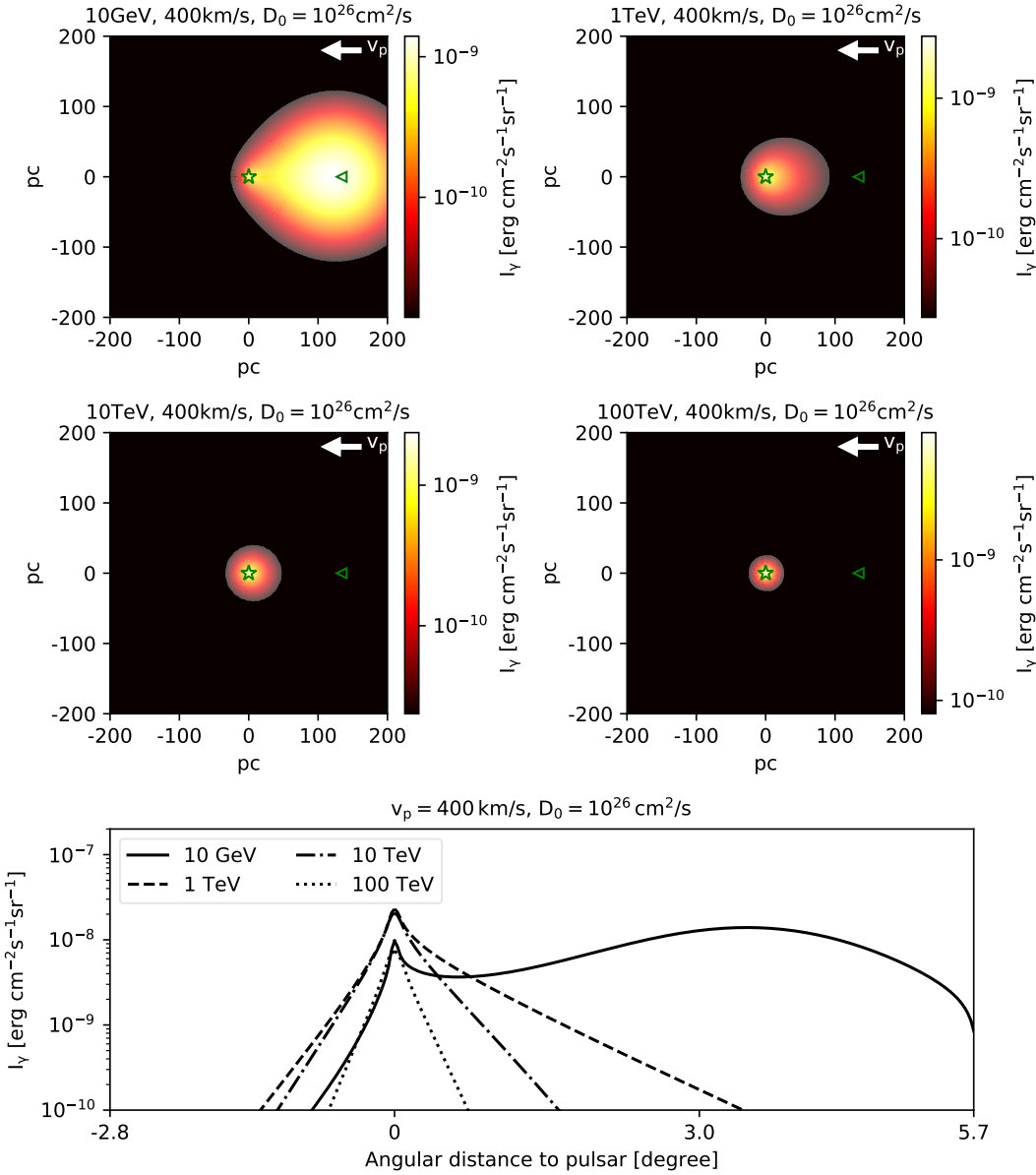


Figure 1. γ -ray intensity morphology of pulsar halo and intensity profile along the axis of pulsar’s proper motion at 10 GeV and 1, 10, 100 TeV, considering the proper motion of a Geminga-like pulsar. The direction of proper motion is marked with the arrow. The star and triangular mark the present and initial position of pulsar. The proper motion velocity is $v_p = 400$ km/s and the diffusion coefficient is $D_0(1 \text{ GeV}) = 10^{26} \text{ cm}^2/\text{s}$.

Table 1. PSF of detectors at different energies.

	E_γ [GeV]	1.6	2.6	5.2	10.4	52
Fermi-LAT	PSF [$^\circ$]	0.4	0.26	0.16	0.1	0.06
HESS	E_γ [TeV]	1.0	3.3	6.6	8.3	16.5
	PSF [$^\circ$]	0.07	0.06	0.05	0.05	0.04
WCDA	E_γ [TeV]	1.0	3.3	6.6	8.3	16.5
	PSF [$^\circ$]	0.6	0.34	0.28	0.27	0.24
KM2A	E_γ [TeV]	16	26	39	59	88
	PSF [$^\circ$]	0.5	0.37	0.3	0.24	0.2

Note—PSF of Fermi-LAT, HESS and LHAASO (WCDA, KM2A).

WCDA. After the convolution, the profile becomes more smooth and extended. Such a change is more pronounced for larger PSF as can be seen by comparing the 1 TeV profile convolved with WCDA’s PSF and that convolved with HESS’s PSF. Also, due to the asymmetric morphology, the position of the intensity peak shifts a little bit to the side of $x > 0$, toward which the halo extends in the intrinsic intensity map. This is apparent for large PSF, as can be seen from the 1 TeV γ -ray profile convolved with WCDA’s PSF.

We find that based on the age of the pulsar, the cooling of emitting electrons, and the velocity of the proper mo-

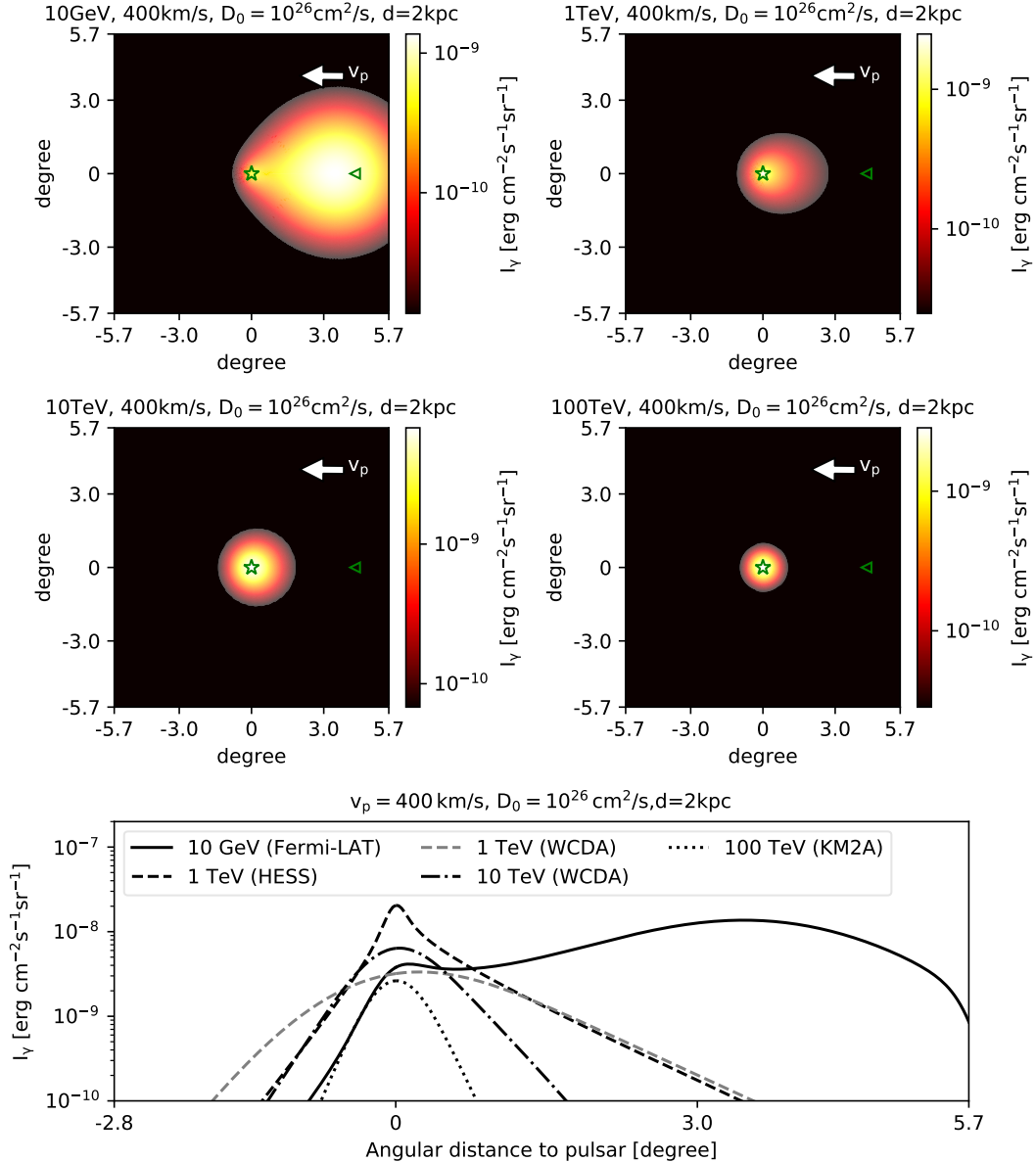


Figure 2. Same as Fig. 1 but after convolving with the PSF of instruments. At four energies we plot, we take the PSF of Fermi-LAT (10 GeV), HESS (1 TeV), WCDA (1,10 TeV) and KM2A (100 TeV), respectively.

tion, the morphological evolution of the pulsar halo can be divided into three phases. Let us first define two critical timescales. One is the time when the electron's diffusion distance $2\sqrt{Dt}$ is equal to pulsar motion distance by $t_{pd} = 80(E_e/1\text{TeV})^{1/3}(v_p/400\text{km/s})^{-2}$ kyr. The other one, denoted by t_c , is the time needed to cool an electron from energy E_c (the cutoff energy in the injection spectrum) to certain energy E_e in the considered magnetic field and the radiation field. t_c can be calculated via Eq. 5. For a fixed magnetic field and radiation field, the value of t_c is generally a few times larger than the standard definition of the cooling timescale $\tilde{t}_c(E_e)$ of electrons (i.e., $\tilde{t}_c \equiv E_e/b(E_e)$). Its value is mainly determined by E_e instead of E_c . Now, the three phases of pulsar halo

evolution can be given by:

PHASE I: $t_{age} < t_{pd}, t_{age} < t_c$. A huge amount of electrons injected at early epoch with a high luminosity haven't cooled and pulsar's displacement due to proper motion is still within the diffusion length of these relic electrons. The relic electrons form a bright region close to the original position of the pulsar. Since relic electrons have diffused to a larger distance than the pulsar has travelled, the superposition of injected electrons at different epoch would yield a single-peaked morphology with a broad peak. The peak position of the intensity profile—whether it is close to the original position or the current position of the pulsar—depends on the relative contribution of relic electrons and newly injected electrons

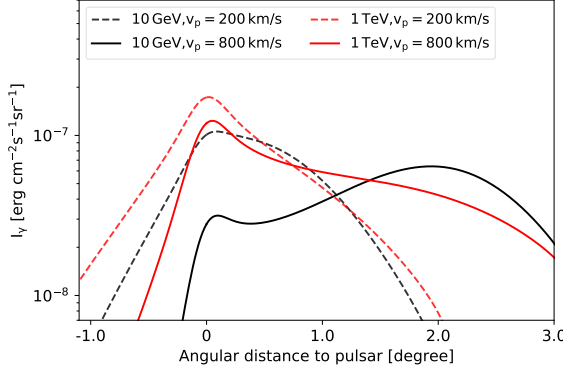


Figure 3. The γ -ray intensity profile of Geminga-like pulsar halo, but with $t_{\text{age}} = 100$ kyr and $v_p = 200$ km/s and 800 km/s, after convolving with the PSF. Other parameters are the same as Fig.2.

which is related to the injection history $L_e(t)$ as will be discussed in the later part of this section.

PHASE II: $t_{\text{pd}} < t_{\text{age}} < t_c$. Since the displacement of the pulsar from its original position is proportional to t while diffusion distance is proportional to $t^{1/2}$, the pulsar eventually goes beyond the diffusing electrons injected initially, and the newly injected electrons form a distinct bright region around $x = 0$. The pulsar halo is highly anisotropic with an extension towards the direction $x > 0$. Again, the relative brightness at the original position of the pulsar and the present position of the pulsar depends on $L_e(t)$.

PHASE III: $t_{\text{age}} > t_c$. Electrons injected at early epoch lost most energy and only recently injected electrons can produce γ -ray emission. The morphology of pulsar halo is again single-peaked at the current position of the pulsar, with a narrow peak and a rough circular symmetry such as the intensity profile of 10 TeV in Fig.2.

Note that at the same age, the pulsar halo could be in different phases at different energies. In the transition regime from one phase to another phase (i.e., $t_{\text{age}} \sim t_{\text{pd}}$, $t_{\text{pd}} \sim t_c$), the feature of a phase mentioned above may not be distinct.

We also check the intensity of the pulsar halo in the benchmark case, but for an age of $t_{\text{age}} = 100$ kyr with $v_p = 200$ km/s and 800 km/s respectively. At this age, the pulsar halo at 10 GeV and 1 TeV with $v_p = 200$ km/s belongs to PHASE I while those with $v_p = 800$ km/s belong to PHASE II, as is shown in Fig.3.

The injection history of pulsar wind $L_e(t)$ also influences the morphology of the pulsar halo, especially at $x > 0$. We compare the cases of a braking index of $n = 1.5$, the case of an initial spindown timescale $\tau_0 = 2$ kyr with the benchmark case in Fig.4, at $t_{\text{age}} = 100$ kyr and $v_p = 400$ km/s for the pulsar. Note that although the initial spindown timescale τ_0 depends on the value of the braking index n , we here simply change the values of these parameters independently in Eq. 2 to illustrate the impact of injection history. It's obvious

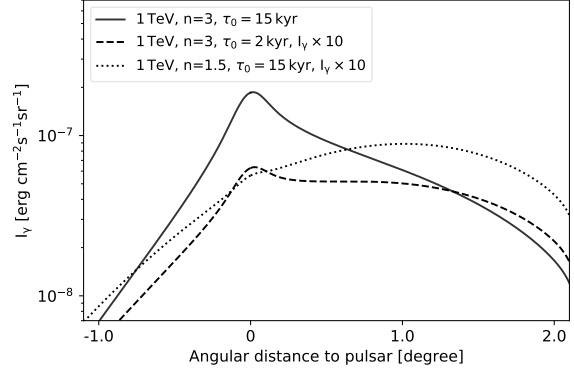


Figure 4. The γ -ray intensity profile of Geminga-like pulsar halo, but with $t_{\text{age}} = 100$ kyr, $\tau_0 = 2$ kyr and $n = 1.5$ in Eq.3, after convolving PSF. Other parameters are the same as Fig.2.

that either a smaller n or a smaller τ_0 lead to a larger ratio between the initial spindown luminosity and the present spindown luminosity of the pulsar, and thus the relative contribution of relic electrons becomes more important (the intensity at $x > 0$ becomes higher). The intensity also peaks away from the present position of the pulsar. This may explain the offsets between the pulsar position and the centroid of the halo seen in some TeV sources at TeV energies.

4. SEPARATION ANGLE ESTIMATION

We now look into the expected offset of the pulsar and the γ -ray halo at different γ -ray energies when measured by different instruments. We first produce PSF-convolved intensity maps at different energies, and convolve 1 – 100 GeV emission with the PSF of Fermi-LAT, 1 – 20 TeV emission with the PSFs of WCDA and HESS respectively, and 10 – 100 TeV emission with the PSF of KM2A. Then, we define two kinds of offsets: one is the separation between the pulsar and the centroid of the halo (denoted by Θ), and the other is the separation between the pulsar and the brightest position of the halo (denoted by Θ'). The latter is straightforward to obtain. To get the former, we use a Gaussian template as $I_G(\mathbf{r}) = (N_0/2\pi\sigma_0^2) \exp[-(\mathbf{r} - \mathbf{r}_c)^2/2\sigma_0^2]$, where \mathbf{r}_c is its center, to model the PSF-convolved γ -ray halo. We set N_0 , σ_0 and \mathbf{r}_c as free parameters, and search for the centroid of the halo (\mathbf{r}_c) by minimizing the chi-square $\chi^2 = \sum_{\mathbf{r}} (I_G - I_{\gamma})^2/I_{\gamma}$.

The obtained separation angles Θ and Θ' at different energies for a Geminga-like pulsar are plotted in Fig.5. At GeV band Θ is basically constant with energy and is close to the displacement of the pulsar due to proper motion in a time of t_{age} , which is $\Theta = 3.8^\circ$ for a nominal distance of 2 kpc of the pulsar. It reflects the emission of the huge amount of relic electrons injected at early epoch (PHASE II). Θ' is also more or less constant at GeV band but jumping to almost zero at 100 GeV. This is because, as the energy increasing, the relic electrons starts to cool, although the relic electrons at this energy still make an important contribution to the entire emis-

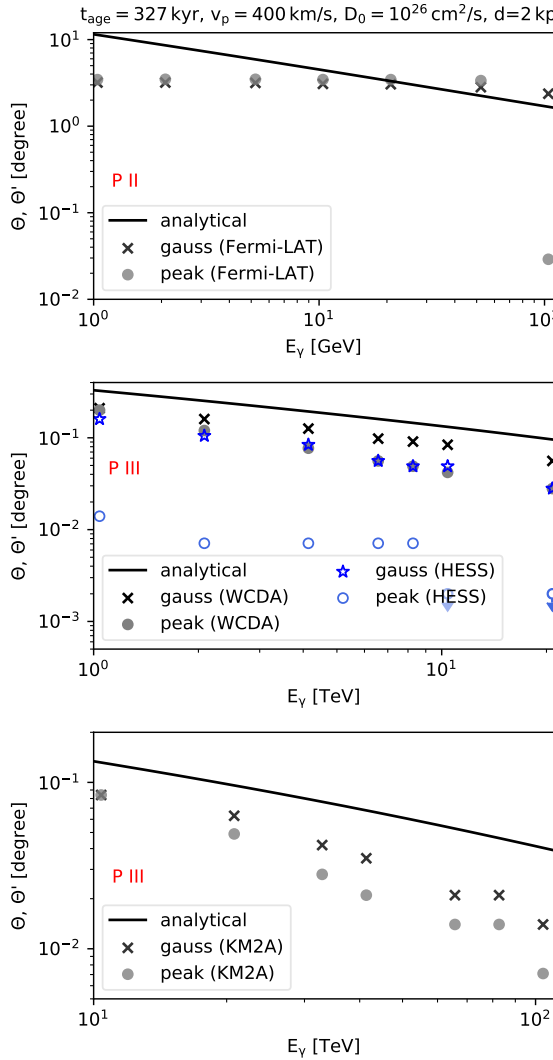


Figure 5. The separation angle Θ defined by modelling Gaussian template (crosses and stars) and Θ' defined as peak of halo (dots and circles) at different energies of Geminga-like pulsar halo. We take PSF of Fermi-LAT for GeV, for 1 – 20 TeV we adopt PSF of WCDA and HESS, and PSF of KM2A for 10 – 100 TeV separately. The black line shows the analytical expectation of Θ' (Di Mauro et al. 2020). We annotate evolutionary phase of pulsar halo in red (i.e., P II for PHASE II and P III for PHASE III).

sion of the pulsar. The expected separation angle is able to be resolved provided that the source is not located too far away (e.g., within several kpc). As energy further goes up, the cooling of emitting electrons becomes increasingly important (PHASE III) and hence the separation, either defined by Θ or Θ' , becomes smaller. Above 10 TeV the separation is smaller than 0.1° and is difficult to be resolved by current gamma-ray instruments especially for those with large PSF such as HAWC and LHAASO.

It is clear that cooling of electrons can reduce the offset be-

cause it reduces the contribution of relic electrons, the distribution of which are not centred at the current position of the pulsar. Di Mauro et al. (2020) suggested that the offset can be analytically depicted by $\Theta(E_\gamma) = \text{atan}(v_p \tilde{t}_c(E_\gamma)/d)$ in the cooling-dominated regime (i.e., PHASE III), where $\tilde{t}_c(E_\gamma)$ is the cooling timescale of electrons that dominates the gamma-ray flux at E_γ . We overlaid the result given by this formula² in Fig. 5 for reference. We see that the formula generally reproduces the trend of Θ v.s. γ -ray energy, but it overestimate the separation angle. This is due to the influence of the continuous injection, which would make the peak position closer to the current position of the pulsar, is not considered in this analytical formula.

Some other parameters can also influence the separation angle. The effects of diffusion coefficient and the proper motion velocity on the offset are important. We check the results with different v_p and D_0 in Fig. 6. With increasing v_p or decreasing D_0 , the pulsar halo at GeV-TeV energy transits from PHASE I to PHASE II gradually. Although the separation angle keeps monotonous increase with the proper motion velocity or monotonous decrease with diffusion coefficient, the slopes are different in the two phases. For example, for halo at 10 GeV, Θ' is close to 0 and do not increase significantly with the velocity of the pulsar’s proper motion at PHASE I while it increases rapidly with the velocity at PHASE II. (see top left panel of Fig. 3). This is because the pulsar has not gone far from the original position and the emission of relic electrons and newly injected electrons are mixed together in PHASE I, and the peak in the intensity map is between the current position and the original position of the pulsar due to the superposition of both two components. On the contrary, in PHASE II, the emission of relic electrons and newly injected electrons are spatially separated while the former one is brighter. Therefore, the intensity peaks locates close to the origin position of the pulsar and the separation angle is almost equal to the displacement of the pulsar.

Another important factor for the morphology of the pulsar halo is the electron injection history $L_e(t)$. As we discussed above, the morphology could be more asymmetric with smaller n and/or τ_0 , and vice versa. For example, the separation angles for a Monogem-like pulsar ($t_{\text{age}} = 109$ kyr and $\tau_0 = 2$ kyr) are plotted in Fig. 7. At several TeV, the pulsar halo just enters PHASE I, the centroid of the pulsar halo is still near the initial position of the pulsar (at $x = 1.15^\circ$), and Θ is much larger than that in the case of a Geminga-like pulsar. Again, we see that the analytical estimation shown as black curves in these figures exceed the numerical results (PHASE III part), due to the ignorance of continuous injection.

We note that in certain condition the influence of the continuous injection could be suppressed. Practically, as the pulsar wind luminosity decreases with time, the maximum energy of

² The formula given by Di Mauro et al. (2020) does not take into account the Klein-Nishina effect which is important at high energy. Here we include the KN effect in the curves.

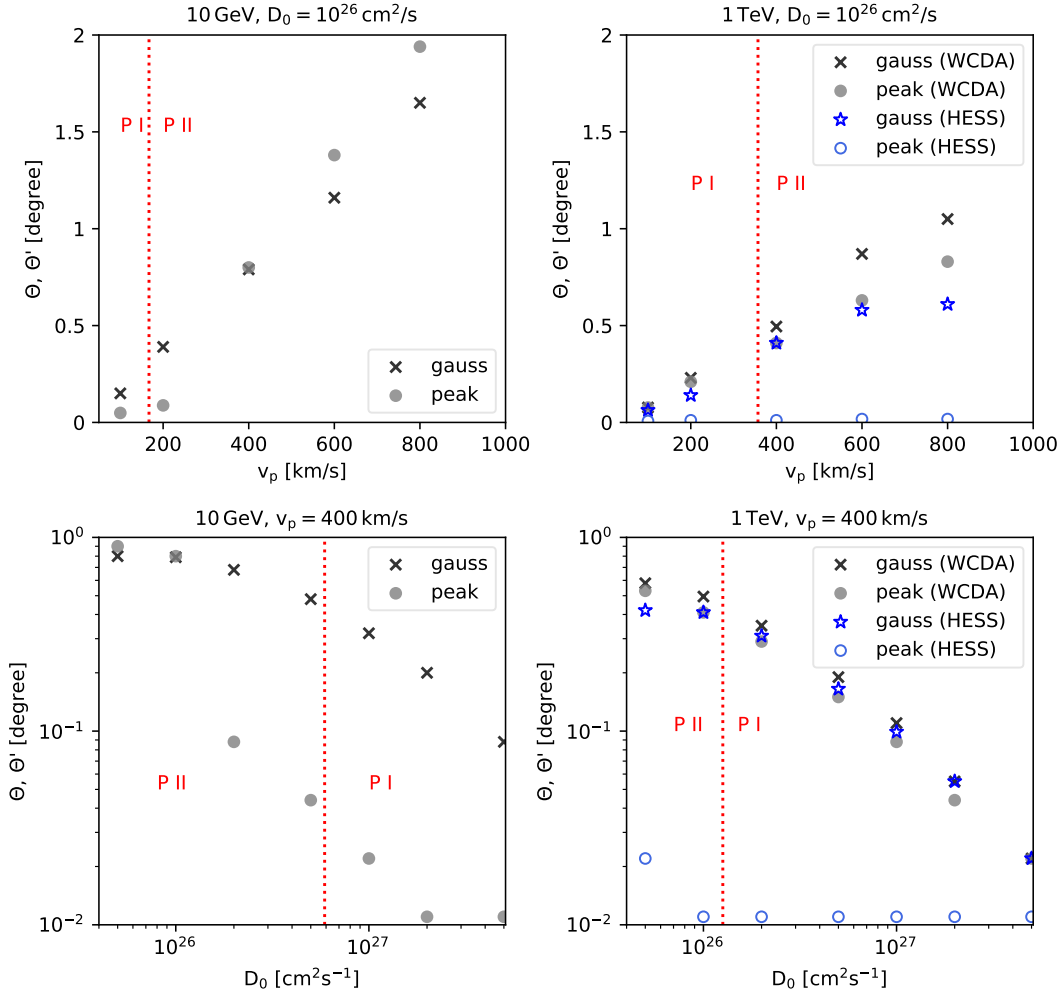


Figure 6. The separation angle Θ and Θ' for different proper motion velocity v_p and diffusion coefficient D_0 at 10 GeV and 1 TeV. The evolutionary phase of pulsar halo is annotated in red and red dotted lines show the boundary between two different phases.

electrons achievable in the termination shock may be also decreasing with time. When the maximum energy decreases below certain energy, we may regard the injection of electrons of this energy being ceased. The termination of injection would cause a larger offset because electrons are not injected at the position close to the present position of the pulsar. However, if the injection stops too early, i.e., the time experienced from the epoch of the injection termination to the present time, denoted by t_s , is longer than the cooling timescale t_c , we do not expect to see the emission of electrons at present. Therefore, we expect the most favorable condition for a large offset to be $t_s \sim t_c$. We then calculate the evolution of the pulsar halo at each energy with turning off the electron injection at $t = t_{\text{age}} - t_c$ to maximize the separation angle. The result is shown in Fig. 8. Note that the offset obtained in this condition (Θ_{max}) is almost independent on the electron injection history. But the velocity of the proper motion is still important and affects the offset by $\Theta_{\text{max}} \propto v_p$. Even in this case, the offset above 100 TeV is still quite small due to the rapid cooling

of ultra-high energy electrons and is difficult to be resolved by the current gamma-ray instrument, i.e., LHAASO-KM2A, unless the pulsar is located sufficient close to Earth (e.g., at a distance of ~ 100 pc from Earth) and has a high proper motion velocity (e.g., > 400 km/s).

5. DISCUSSION

In our calculation of electrons diffusion, we consider a spatially homogeneous diffusion coefficient around the pulsar at a scale of ~ 100 pc. Some previous studies suggest that there could exist two diffusion zones in this region, with a slow diffusion zone within a few tens of parsecs around the pulsar and a normal diffusion zone beyond the radius (Fang et al. 2018; Profumo et al. 2018; Tang & Piran 2019). Our present numerical treatment cannot deal with two-diffusion zones with the proper motion of pulsar, because the diffusion would become highly anisotropic if the pulsar has moved close to the boundary between the slow diffusion zone and the normal diffusion zone. Nevertheless, we may infer the influence of two diffu-

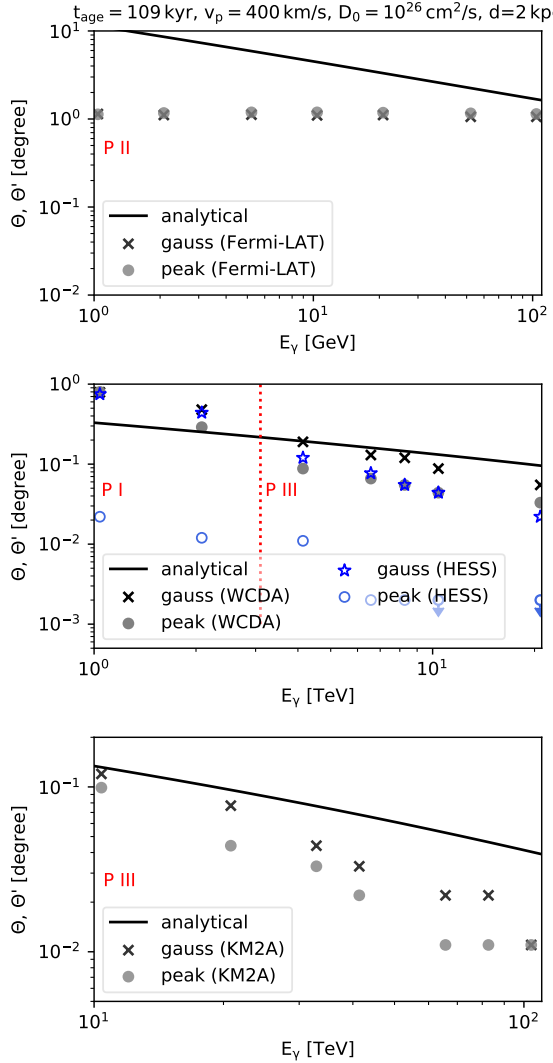


Figure 7. The separation angle Θ and Θ' at different energies of Monogem-like pulsar halo. We take the same PSF as in Fig.5. The evolutionary phase of pulsar halo is annotated in red, while the dotted red line in the middle panel shows the boundary between PHASE I (P I) and PHASE III(P III).

sion zones qualitatively, if the size of the slow diffusion zone is close to the displacement of the pulsar due to proper motion $v_p t_{\text{age}} = 80(v_p/400 \text{ km s}^{-1})(t_{\text{age}}/200 \text{ kyr}) \text{ pc}$. Given the slow diffusion coefficient, a large fraction of the huge amount of electrons injected at early epoch would be still confined inside the slow diffusion zone if not cooled. On the other hand, the electrons injected recently would more likely diffuse in the normal diffusion zone, and leads to a comparatively low particle density around the current position of the pulsar. As a consequence, it is beneficial to yield a large offset.

As we discussed above, it is increasingly difficult to produce resolvable offset between the center of the pulsar halo and the pulsar by the proper motion at higher energy, unless the pulsar is located close-by and the proper motion veloc-

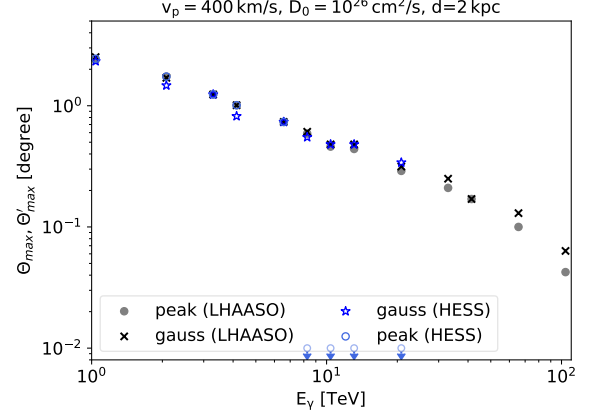


Figure 8. The maximum separation angle Θ_{max} and Θ'_{max} at different energies that can be produced by pulsar proper motion with $v_p = 400 \text{ km/s}$.

ity is high. However, offsets at such a high energy between extended TeV sources and the positions of associated middle-aged pulsars have already been observed by HAWC, and the distances of some candidate pulsars are not that small. If these sources are truly pulsar halos, we have to resort to more complicated but probably realistic framework of particle propagation, such as the anisotropic diffusion with considering the geometric configuration of the magnetic field in the surrounding ISM of the pulsars (Liu et al. 2019b). Let us envisage a specific scenario that the magnetic field in the east side of a pulsar is largely parallel to the periphery of the PWN while in the west side is largely radial. The diffusion of escaping electrons towards east is then suppressed because the cross-field diffusion is slow, while the electrons can quickly diffuse towards west. The pulsar halo under such a configuration of magnetic field would appear significant extension toward the west side and a large offset is expected between the pulsar and the centroid of the halo. Nevertheless, the observed sources of large offsets beyond 10 TeV are not necessarily pulsar halos. With certain specific conditions, a ~ 10 kyr-aged PWN could vigorously expand (Khangulyan et al. 2018) while the asymmetric reverse shock arising from the supernova ejecta could crush one side of the PWN (Blondin et al. 2001; Gaensler et al. 2003; Aharonian et al. 2006), and/or electrons preferentially escape from one side of the PWN due to the geometry of the magnetic field in the PWN (Liu & Yan 2020). These scenarios might cause a significant offset between the centroid of the TeV emission and the pulsar’s location. The source could be even composed of a few different sources. Multiwavelength observations with high angular resolution may help to reveal the true nature of the sources.

6. CONCLUSIONS

In this paper, we studied the γ -ray morphology of a pulsar halo and the spatial offset between the halo and its associated pulsar considering the pulsar’s proper motion. We found

that the evolution of the pulsar halo can be divided into three phases, based on three timescales, namely, when the displacement of the pulsar equal to the diffusion length of the initially injected particle t_{pd} , the cooling timescale of electrons t_c , and the age of the pulsar t_{age} . For pulsar with $t_{\text{age}} < t_{\text{pd}}$ and $t_{\text{age}} < t_c$, the pulsar halo would appear a single-peaked morphology with a broad peak (PHASE I). For $t_{\text{pd}} < t_{\text{age}} < t_c$, the morphology of the pulsar would show significant asymmetry with two humps or one hump with an extended plateau (PHASE II). For $t_c < t_{\text{age}}$, the morphology becomes single-peaked again but with a narrow peak centred at the current position of the pulsar (PHASE III). Our results may provide constraints on the theoretical explanation of the asymmetrical morphology of the pulsar halos at GeV-TeV band.

We define two kinds of offsets between the pulsar halo and the pulsar: one is the separation between the centroid of the halo and the pulsar's position (Θ) and the other is the separation between the brightest position in the halo and the pulsar's position (Θ'). The influence of various model parameters on the separation angles are studied. We found that both separation angles generally decrease with increasing γ -ray energy and becomes difficult to be resolved above 10 TeV. Above 100 TeV, where LHAASO may perform sensitive detection, we do not expect resolvable offset for a pulsar halo due to very rapid cooling of the emitting electrons, unless the pulsar is located in proximity to Earth (e.g., $\lesssim 100$ pc) and/or has a high proper motion velocity (> 400 km/s). On the other hand, if the offset is detected while neither of the two conditions is satisfied, it would require the consideration of a more complex configuration of the magnetic field and correspondingly anisotropic diffusion of electrons. Alternatively, it might imply that the source is not simply a pulsar halo. Multi-wavelength observation with high angular resolution would then be helpful to reveal the true origin of the γ -ray source.

REFERENCES

Abdo, A. A., Allen, B. T., Aune, T., et al. 2009, *ApJL*, 700, L127
 Abeysekara, A. U., Albert, A., Alfaro, R., et al. 2017, *Science*, 358, 911
 —. 2018, *J. Cosmology Astropart. Phys.*, 2, 049
 Aharonian, F., Akhperjanian, A. G., Bazer-Bachi, A. R., et al. 2006, *A&A*, 460, 365
 Aharonian, F. A., Akhperjanian, A. G., Bazer-Bachi, A. R., et al. 2005, *A&A*, 442, L25
 Albert, A., Alfaro, R., Alvarez, C., et al. 2020, arXiv e-prints, arXiv:2007.08582
 Bai, X., Bi, B. Y., Bi, X. J., et al. 2019, arXiv e-prints, arXiv:1905.02773
 Blondin, J. M., Chevalier, R. A., & Frierson, D. M. 2001, *ApJ*, 563, 806
 Bucciantini, N., Blondin, J. M., Del Zanna, L., & Amato, E. 2003, *A&A*, 405, 617
 de Jager, O. C., & Djannati-Ataï, A. 2009, in *Astrophysics and Space Science Library*, Vol. 357, *Astrophysics and Space Science Library*, ed. W. Becker, 451
 Di Mauro, M., Manconi, S., & Donato, F. 2019, *Phys. Rev. D*, 100, 123015
 —. 2020, *Phys. Rev. D*, 101, 103035
 Fang, K., Bi, X. J., Yin, P.-F., & Yuan, Q. 2018, *ApJ*, 863, 30
 Gaensler, B. M., Schulz, N. S., Kaspi, V. M., Pivovaroff, M. J., & Becker, W. E. 2003, *ApJ*, 588, 441
 Gaensler, B. M., & Slane, P. O. 2006, *ARA&A*, 44, 17
 H. E. S. S. Collaboration, Abramowski, A., Acero, F., et al. 2012a, *A&A*, 545, L2
 —. 2012b, *A&A*, 541, A5
 H. E. S. S. Collaboration, Abdalla, H., Abramowski, A., et al. 2018a, *A&A*, 612, A1
 —. 2018b, *A&A*, 612, A2
 Khangulyan, D., Koldoba, A. V., Ustyugova, G. V., Bogovalov, S. V., & Aharonian, F. 2018, *ApJ*, 860, 59
 Liu, R.-Y., Ge, C., Sun, X.-N., & Wang, X.-Y. 2019a, *ApJ*, 875, 149
 Liu, R.-Y., & Yan, H. 2020, *MNRAS*, 494, 2618
 Liu, R.-Y., Yan, H., & Zhang, H. 2019b, *Phys. Rev. Lett.*, 123, 221103
 López-Coto, R., & Giacinti, G. 2018, *MNRAS*, 479, 4526
 Popescu, C. C., Yang, R., Tuffs, R. J., et al. 2017, *MNRAS*, 470, 2539
 Profumo, S., Reynoso-Cordova, J., Kaaz, N., & Silverman, M. 2018, *Phys. Rev. D*, 97, 123008
 Reynolds, S. P., & Chevalier, R. A. 1984, *ApJ*, 278, 630
 Tang, X., & Piran, T. 2019, *MNRAS*, 484, 3491
 Truelove, J. K., & McKee, C. F. 1999, *ApJS*, 120, 299
 van der Swaluw, E., Achterberg, A., Gallant, Y. A., & Tóth, G. 2001, *A&A*, 380, 309